Article

An Open-Circuit Fault Diagnosis Method for LLC Converters

Shibo Xiong [ID], Yuxuan Pei, Weikang Wang, Wenwei Liu *, Peng Zhang and Yang Liu [ID]

Guangdong Provincial Key Laboratory of Electronic Information Products Reliability Technology, No. 76,
West Zhucun Avenue, Guangzhou 511370, China; xshibo@hust.edu.cn (S.X.); peiyuxuan@trinova-tech.com (Y.P.);
weikangwang@foxmail.com (W.W.); pengzhang0611@163.com (P.Z.); yangliu30@gmail.com (Y.L.)
* Correspondence: wenwei2009@163.com

Abstract: In electrified transportation systems, power system failures can lead to greater disasters. Therefore, the reliability of converters in transportation systems has been a concern. Fault-tolerant techniques are widely applied to ensure that converters can continue to supply loads under fault conditions. Fault diagnosis as a prerequisite for fault tolerance has also become a research hotspot. This paper proposes a fast method for fault diagnosis of high-frequency LLC converters. The proposed fault diagnosis method is based on the observation of the voltage across the resonant capacitor to determine and locate the faulty power switch, providing a basis for fault tolerance. This diagnosis method requires a voltage sensor, which is also necessary for some control methods. When applying these control methods, the proposed fault diagnosis method can be used without additional sensors, beneficial for cost reduction. A full-bridge LLC converter controlled by a digital signal processor was used as an experimental platform to verify the effectiveness and speed of the proposed diagnostic method. The results show that the proposed fault diagnosis method can achieve the fast diagnosis of high-frequency LLC converters in a short time and with only minimal computational resources.

Keywords: LLC converter; open-circuit fault; fault diagnosis; resonant capacitor voltage

1. Introduction

As electrification in transportation advances, the significance of DC–DC converters escalates. While a conservative design enhances reliability, it is impractical due to power density and cost constraints. Redundancy, both at the module and switch levels, although effective, compromises power density and incurs high costs due to parallel connections. A more viable solution is fault-tolerant operation, particularly for systems with stringent cost, volume, and weight limitations [1]. This operation encompasses fault diagnosis and isolation [2,3], with the former being a prerequisite for the latter and crucial for practical implementation [2,3]. Hence, this paper concentrates on the fault diagnosis of DC–DC converters.

Power devices, susceptible to electrical and thermal stresses [4], are prone to failures, primarily open-circuit faults (OCF) and short-circuit faults (SCF) [5,6]. SCFs can induce destructive overcurrents, necessitating immediate isolation to prevent system paralysis or destruction. Mature techniques for handling SCFs are integrated into the gate driver's standard features for practical applications [7,8]. Additionally, hardware protection circuits, such as fuses, convert SCFs into OCFs to prevent converter damage [9]. OCFs, however, overstrain healthy devices and cause pulsating current. In MOSFETs, switch failures primarily result from gate-oxide degradation, bond wire degradation, and die attach solder cracks and delamination [10–12]. Given their concealed nature compared to SCFs, there is a demand for rapid and accurate OCF diagnosis methods.

Open-Circuit Fault (OCF) diagnosis methods are generally classified into three categories: signal-based, model-based, and data-based methods [13]. Signal-based fault diagnosis methods measure specific signals containing fault information and extract features for diagnosis. Typical signals include inductor currents [14], inductor voltages [15],

and DC bus currents [16]. In [14], faulty switches were localized within 0.4 ms by monitoring the PWM pulses' rising and falling edges for each phase inductor current. In [15], faults in switches and diodes of Boost converters were diagnosed using inductor voltage polarity and drive signals. In [16], OCF was diagnosed utilizing DC bus current derivatives.

Model-based fault diagnosis methods substitute hardware redundancy with computational redundancy. Various observers, including sliding mode observers [13], state estimators [17], and adaptive gradient descent algorithms [18], are applied to fault diagnosis. In [13], a sliding mode observer-based fault diagnosis method for power switch OCFs was proposed. In [17], a generalized fault diagnosis method was proposed after analyzing, designing, and experimentally verifying various types of converters using a model-based state estimator method.

Data-based fault diagnosis methods leverage artificial intelligence techniques and large volumes of historical data to train expert diagnosis systems. With advancements in machine learning algorithms and computational power, various deep learning network algorithms, such as back-propagation neural networks [19] and extreme learning machines [20], have been applied to the fault diagnosis of power electronic converters. These methods do not require modeling, fault analysis, or rule formulation, but they necessitate substantial training data and computation. Most data-based fault diagnosis methods are challenging to apply to real-time fast fault diagnosis.

The rising switching frequency enhances the appeal of the LLC converter, renowned for its high efficiency, power density, electrical isolation, low electromagnetic interference, and high operational frequency. Despite its widespread application, research on LLC converter fault diagnosis is sparse. Typical OCF diagnostic strategies utilize the bridge arm midpoint voltage as the fault signal for detection. However, this approach necessitates the installation of a voltage sensor at each converter bridge arm's midpoint and tends to have a relatively complex computation [21]. This study introduces a two-step, signal-based OCF diagnostic method for LLC converters, suitable for high-frequency applications due to its minimal computational and sampling resource requirements. The method involves sensing the resonant capacitor voltage, comparing it with a reference value for a general fault indication, and employing a fault injection strategy to pinpoint the faulty switch. Fault injection is achieved by temporarily modifying the modulation module's switching signals. The method's advantages include low cost, simple circuit design, and high reliability, requiring minimal sensors and components, some of which are already present in certain control methods.

This paper is organized as follows. The structure and operation principles of the LLC converter are introduced in Section 2. The operation process under fault condition is analyzed, and the feature extraction is illustrated in Section 3, and the fault injection strategy is given to locate the faulty switch. The experimental results are presented to verify the feasibility of the proposed method in Section 4, and a conclusion is drawn in Section 5.

2. System Overview

2.1. Basic Operation of the LLC Converter

The conventional full-bridge LLC converter is shown as Figure 1. The converter consists of power switches S_{1-4}, freewheeling diodes D_{1-4}, a resonant tank, and rectifier diodes D_{5-8}. The resonant tank includes a resonant inductor L_r, a resonant capacitor C_r, and a magnetizing inductor L_m. The output capacitor C_o filters the rectified current and stabilizes output voltage for the load R_o. The LLC converter is usually designed to be operated lower and near the resonant frequency. The waveforms can be obtained as Figure 2, and the operation waveforms can be divided into six stages in a switching period. Stage 1, 4 show resonance with L_r and C_r. Stage 2, 5show resonance with L_m, L_r and C_r. Stage 3, 6 represent dead-time durations.
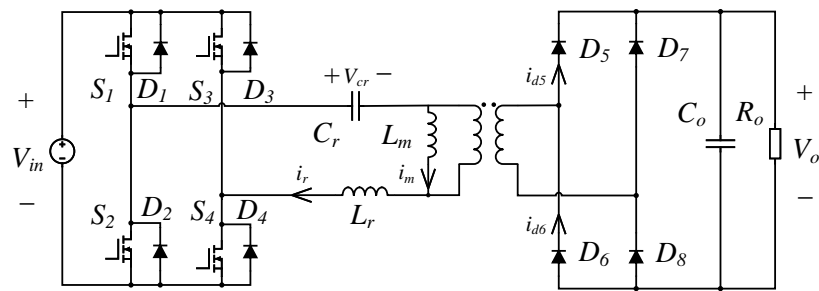
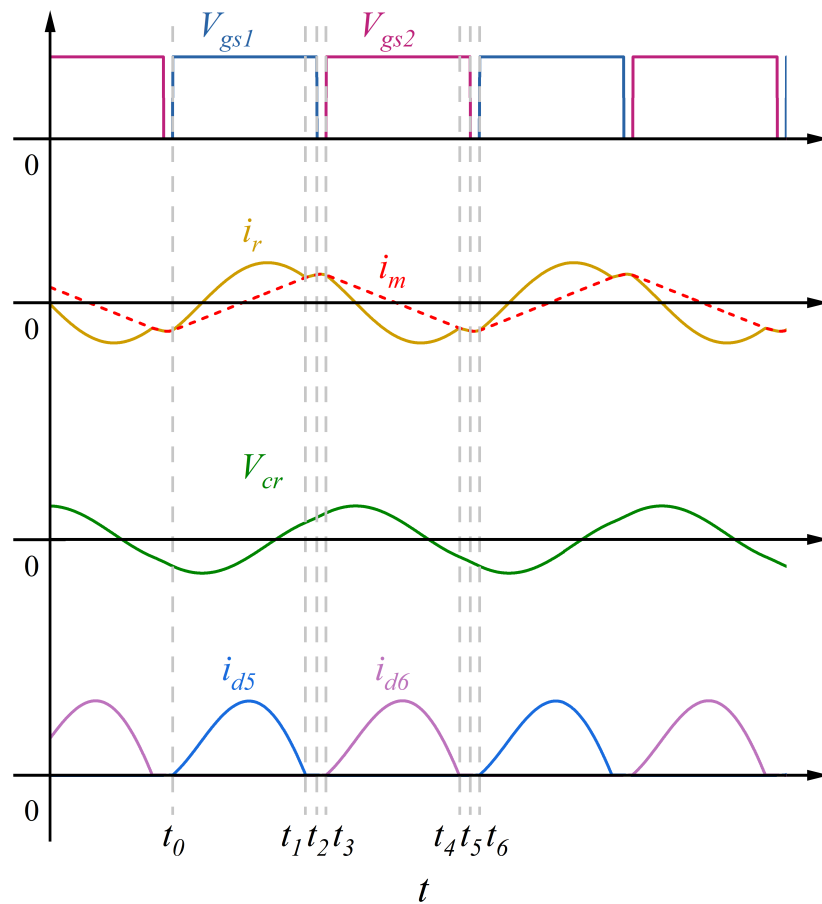**Figure 1.** The typical structure of full-bridge LLC converter.

Figure 2. The waveforms of the full-bridge LLC converter in condition.

Stage 1 [$t_0 < t < t_1$]: Since resonant current i_r is lower than 0 before $t = t_0$, i_r flows through diodes $D_{1,4}$, which makes the drain-source voltage V_{ds} of $S_{1,4}$ clamped at $-V_F$, where V_F is the forward conduction voltage drop of the freewheeling diode. Therefore, ZVS for $S_{1,4}$ is achieved at $t = t_0$. During this stage, power is transferred to the secondary side through the transformer. On the secondary side, D_5 is forward conducting and D_6 is reversely biased. The voltage across the transformer secondary side is clamped at the output voltage V_o, so the voltage across the magnetizing inductor L_m remains NV_o. Magnetizing current i_m increases linearly with the slope rate of NV_o/L_m. Resonant current i_r flows through MOSFETs S_1 and S_4, fluctuating in sinusoidal form. Therefore, the resonant current $i_r(t)$, the resonant capacitors voltage $V_{cr}(t)$, the magnetizing current $i_m(t)$, and the secondary current $i_{d5}(t)$ can be given as follows:

$$\begin{aligned} i_r(t) = C_r\omega_{r1}(V_{in} - V_{1,ini} - NV_o)\sin(\omega_{r1}t) \\ + I_{1,ini}\cos(\omega_{r1}t) \end{aligned} \tag{1}$$

$$V_{cr}(t) = V_{in} - NV_o - (V_{in} - NV_o - V_{1,ini}) \cos(\omega_{r1} t)$$
$$+ \frac{I_{1,ini}}{C_r \omega_{r1}} \sin(\omega_{r1} t) \tag{2}$$

$$i_m(t) = \frac{NV_o(t - t_0)}{L_m} + I_{1,ini} \tag{3}$$

$$i_{d5}(t) = N[i_r(t) - i_m(t)] \tag{4}$$

where $I_{1,ini}$ and $V_{1,ini}$ is the initial value of resonant current i_r and resonant capacitor voltage V_{cr} at $t = t_0$, $\omega_{r1} = 2\pi f_{r1} = \frac{1}{2\pi\sqrt{L_r C_r}}$.

Stage 2 [$t_1 < t < t_2$]: At $t = t_1$, $i_r(t)$ and $i_m(t)$ become equal, while the energy transmission between the primary side and the secondary side is terminated. Diode current i_{d5} drops to zero, so ZCS for $D_{5,8}$ is achieved. Magnetizing inductance L_m participates in the resonance between L_r and C_r. Due to L_m is much larger than L_r, resonance angular velocity ω_{r2} in Stage 2 is much less than ω_{r1} in Stage 1. Therefore, i_m and i_r are approximately unchanged at this time. The resonant capacitor is charged by the approximately constant current and V_{cr} rises approximately linearly. Therefore, the resonant current $i_r(t)$, the resonant capacitors voltage $V_{cr}(t)$, the magnetizing current $i_m(t)$, and the secondary current $i_{d5}(t)$ can be derived as follows:

$$i_r(t) = i_m(t) = \sqrt{\frac{C_r}{L_m + L_r}}(V_{in} - V_{2,ini}) \sin[\omega_{r2}(t - t_1)]$$
$$+ I_{2,ini} \cos[\omega_{r2}(t - t_1)] \tag{5}$$

$$V_{cr}(t) = V_{in} + (V_{2,ini} - V_{in}) \cos[\omega_{r2}(t - t_1)]$$
$$+ \sqrt{\frac{L_m + L_r}{C_r}} I_{2,ini} \sin[\omega_{r2}(t - t_1)] \tag{6}$$

$$\omega_{r2} = 2\pi f_{r2} = \frac{1}{\sqrt{(L_r + L_m)C_r}} \tag{7}$$

$$i_{d5}(t) = N[i_r(t) - i_m(t)] = 0 \tag{8}$$

where $I_{2,ini}$ and $V_{2,ini}$ is the initial value of resonant current i_r and resonant capacitor voltage V_{cr} at $t = t_1$. Due to the waveforms of i_r, i_m and V_{cr} are symmetrical, it can be derived as follows:

$$I_{1,ini} = -I_{2,ini} = -\frac{NV_o T_r}{4L_m} \tag{9}$$

where T_r is the resonance period of L_r and C_r and equals $1/f_{r1}$.

Stage 3 [$t_2 < t < t_3$]: At $t = t_2$, $S_{1,4}$ are turned off. The current of resonant tank i_r cannot drop to zero immediately because of the inductance. So, $D_{2,3}$ start freewheeling. There is still no energy transmission from the primary side to the secondary side, so i_r and i_m remain equal. The conducting of $D_{2,3}$ making $S_{2,3}$ clamped, ready to be turned on with ZVS.

Stage 4–6 [$t_3 < t < t_6$]: During these stages, S_{1-4} respectively perform the opposite operation of Stage 1–3. Resonant current i_r, magnetizing current i_m and resonant capacitor voltage V_{cr} are equal to those in Stage 1–3 , but in opposite directions. Diode current i_{d6} repeats the change during Stage 1–3 of i_{d5}.

Through the above analysis about steady-state operating process, it can be seen that during the Stage 4–6, energy transmission only happens in the Stage 1,4. The average value of the rectifier output current i_o in a cycle T_s ($T_s = 1/f_s$) is equal to I_{oa}, which can be expressed as

$$\int_{t_0}^{t_1} i_o(t)dt = \int_{t_0}^{t_1} N[i_r(t) - i_m(t)]dt = \frac{T_s I_{oa}}{2} \tag{10}$$

when the load is determined. $V_{1,ini}$ in (1) can be derived based on (10), which is as follows:

$$V_{1,ini} = -\frac{I_{oa}}{4Nf_l C_r} - \frac{NV_o(f_l - f_{r1})}{16L_m f_{r1} C_r} \tag{11}$$

2.2. The LLC Converter after an OCF

In fact, the full-bridge LLC converter can continue to output power with an OCF on a power switch. As shown in Figure 3, the converter is still operating with an OCF on S_4. Therefore, V_{gs4} is always pulled down to simulate the OCF. It is imperative to highlight that the symmetrical architecture of the LLC converter implies that a comparable event would transpire if any power device were to malfunction. For the purpose of this discussion, we exemplify this scenario by pulling down V_{gs4}. However, there are differences between before and after the OCF. A operating cycle after the OCF can be divided into seven stages. Some stages are similar to those before the OCF.
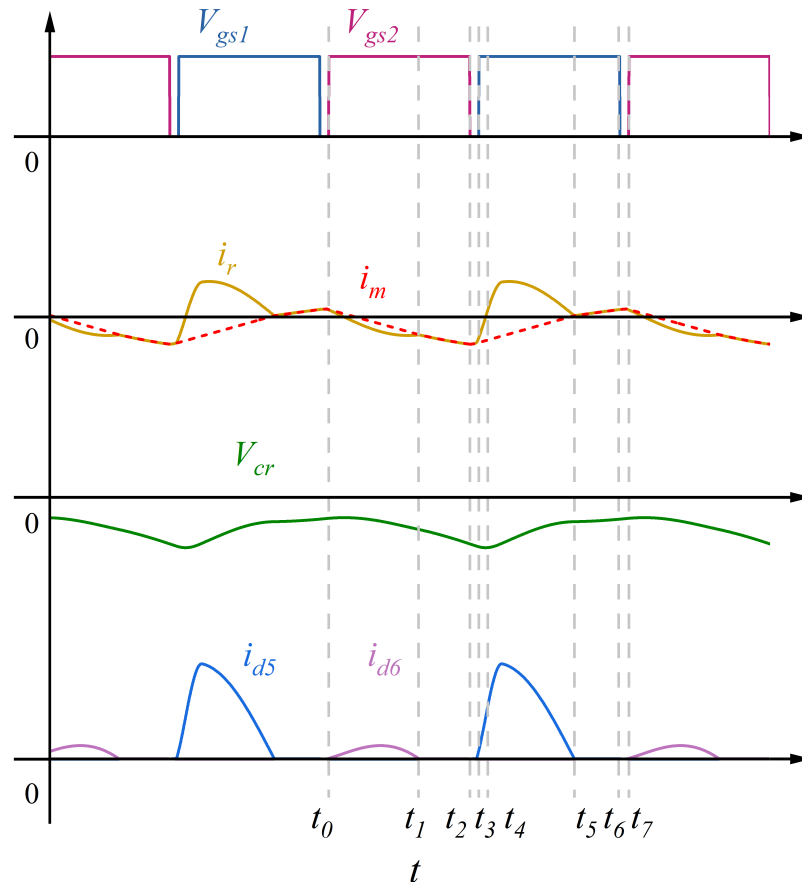

Figure 3. The waveforms of the full-bridge LLC converter with an OCF on S_4.

Stage 1 [$t_0 < t < t_1$]: At $t = t_0$, $S_{2,3}$ are turned on with ZVS. L_r and C_r begin resonance. The transformer primary side is clamped, and the magnetizing current i_m drops linearly, as normal.

Stage 2 [$t_1 < t < t_2$]: i_m drops until i_m equals i_r at $t = t_1$. Then the energy transmission is interrupted. i_m and i_r drop slowly due to the resonance of L_r, L_m, and C_r. V_{cr} drops almost linearly.

Stage 3 [$t_2 < t < t_3$]: At $t = t_2$, all power switches are off. i_r starts to discharge $C_{oss1,4}$ and charge $C_{oss2,3}$, where C_{ossx} is the parasitic capacitor of S_x. When the charge on $C_{oss1,4}$ is released, the current begins to flow through the freewheeling diodes.

Stage 4 [$t_3 < t < t_4$]: At $t = t_3$, $V_{gs1,4}$ is pulled up. However, S_4 cannot be turned on because of the OCF. Therefore, i_r flows through D_4 and feeds back energy to the power supply V_{in}, which results in i_r rising sharply. Due to the recovery of energy transmission, $V_p = NV_o$ and i_m rises linearly.

Stage 5 [$t_4 < t < t_5$]: The primary side continues to supply energy to the secondary side until i_r drops to 0 at $t = t_4$. Then the direction of i_r is reversed. C_r releases the stored charge, and together with V_{bus} discharges C_{oss5} and charges C_{oss6}. This process continues

until C_{oss5} releases the charge, then D_5 is conducted, and the resonant tank continues to supply energy to the secondary side through the S_3 and D_5.

Stage 6 [$t_5 < t < t_6$]: At $t = t_5$, i_r equals i_m, and energy the transmission ends. L_r, L_m and C_r begin to resonate together.

Stage 7 [$t_6 < t < t_7$]: At $t = t_6$, $V_{gs1,4}$ are pulled down, and the converter enters the dead zone again. i_r starts to charge or discharge C_{oss1-4}.

It can be seen that the faulty converter behaves like a half-bridge LLC converter. About half of input voltage become the bias voltage on C_r, and output voltage V_o drops by half. This once again demonstrates the concealment of OCF and the importance of timely discovery. However, these are the waveforms after the converter is stabilized again after an OCF occurs. When the OCF occurs, the system will enter a transient state until V_o drops. As shown in Figure 4, the time t_f when the OCF occurs is marked with red dotted lines. Since the faulty converter cannot maintain the original output voltage, the converter can hardly output energy for the secondary side, and the load only relies on the output capacitor C_o to supply energy until V_o drops to half. During this period, a bias voltage is generated on C_r, and V_{cr} is no longer reversed.
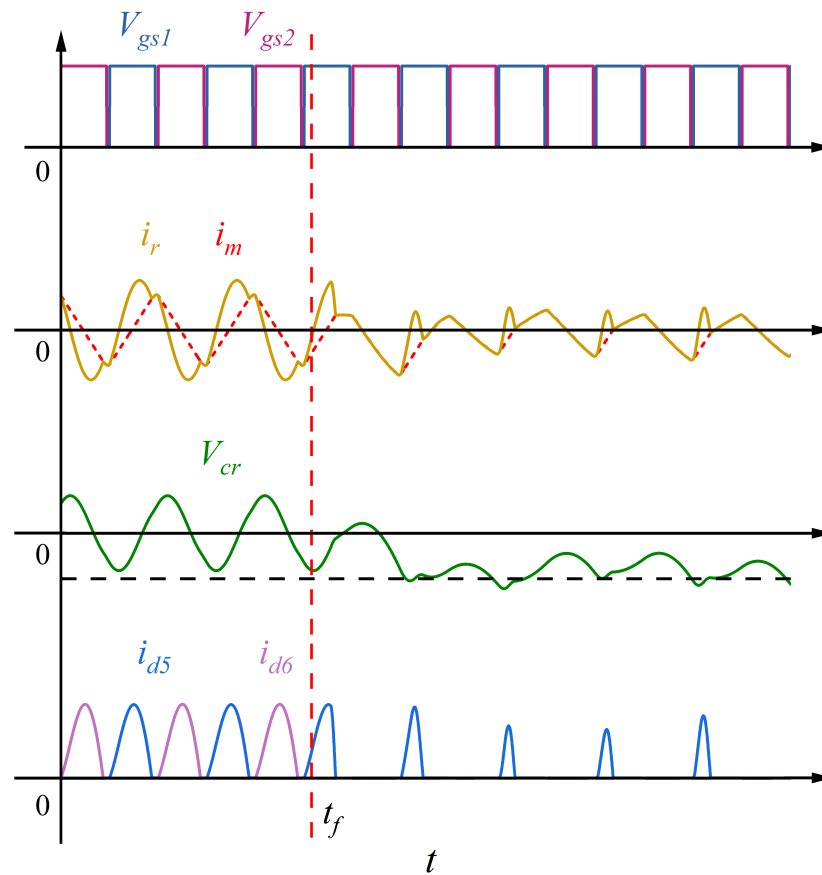

Figure 4. The waveforms of the full-bridge LLC converter in the transition process.

3. Fault Diagnose Strategy of The LLC Converter

3.1. Diagnostic Signal Selection

V_{cr} is the integral of i_r, and V_{cr} change periodically with i_r in steady state. Therefore, when i_r crosses zero, V_{cr} reaches the maximum or minimum value. However, when the load is different, the time of i_r zero crossing is also different. The output current depends on the difference between i_m and i_r, as shown in the gray line filled part in Figure 5. i_m is not affected by the load and always crosses zero at the middle of the pulse t_{mid}. When the load is extremely light, the curve of i_r is infinitely close to that of i_m, and the zero-crossing time t_{zeo} of i_r is close to t_{mid}. Therefore, $V_{cr}(t_{beg})$ is approximately equal to 0 in light load

due to the symmetry. And the heavier the load, the faster the i_r will cross zero. Therefore, $V_{cr}(t_{beg})$ is close to $V_{cr}(t_{zeo})$ in heavy load.
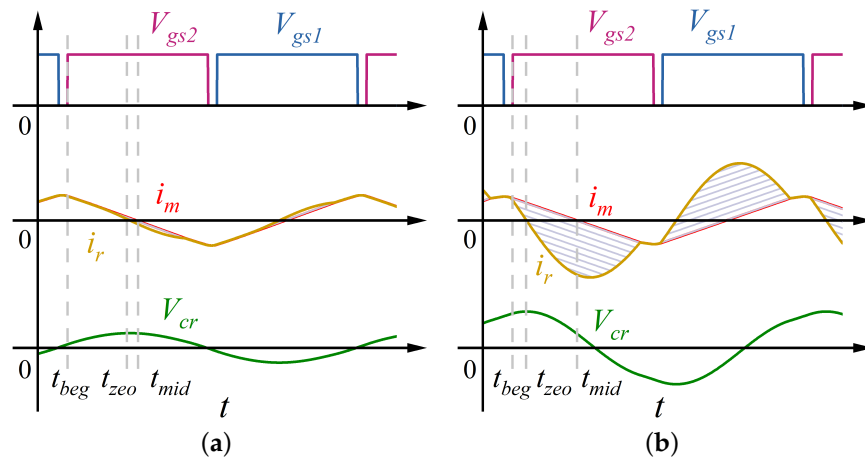

Figure 5. The relationship between resonant capacitor voltage V_{cr} and the sampling time: (**a**) in light load (**b**) in heavy load.

To locate the faulty switch of a high-frequency converter, the signal $V_{cr}(t_{beg})$ with adequate information is selected. This can effectively reduce the number of samples per cycle and relieve the pressure of DSP sampling and calculation. If an OCF occurs, it will be reflected in V_{cr} soon. This helps to find the OCF faster. It is worth noting that many control methods take V_{cr} as a control variable [22,23]. Therefore, the proposed method has little cost for these control methods.

3.2. Fault Diagnose Strategy

The proposed fault diagnosis strategy shown in Figure 6 will be illustrated based on the LLC converter with parameters as shown in Table 1. It should be noted, however, that this strategy is not limited to these specific parameters and can be adapted to LLC converters with different characteristics. As the load increases, the amplitude of $V_{cr}(t_{beg})$ increases from about 0. However, no matter how heavy the load is, $V_{cr}(t_{beg1})$ at the pulse starting time of V_{gs1} is always negative, while $V_{cr}(t_{beg2})$ at the pulse starting time of V_{gs2} is always positive. This conclusion can also be derived from (11). When the OCF occurs, $V_{cr}(t_{beg})$ no longer fluctuates around zero point, but changes to fluctuate around $+\frac{V_{in}}{2}$ or $-\frac{V_{in}}{2}$. Therefore, the OCF can be diagnosed by monitoring the direction of $V_{cr}(t_{beg})$ shown in Figure 7. V_{cr} is sampled twice per cycle, at the beginning of two driver signal pulses respectively, and converted into a logical signal S_{vcr}

$$\begin{cases} V_{cr}(t_{beg}) > +V_{thd}, & S_{vcr} = 1 \\ V_{cr}(t_{beg}) < -V_{thd}, & S_{vcr} = -1 \\ -V_{thd} < V_{cr}(t_{beg}) < +V_{thd}, & S_{vcr} = 0 \end{cases} \tag{12}$$

where the threshold voltage V_{thd} is set to prevent misdiagnosis caused by zero crossing oscillation, sampling error and other factors during light load. Therefore, in normal operation, the sampled $V_{cr}(t_{beg})$ of each cycle can as shown in the Table 2.

When $V_{cr}(t_{beg1})$ and $V_{cr}(t_{beg2})$ are both 1 or -1, it is deemed that an OCF happens and the fault signal $flag_{vcr}$ changes from 0 to 1 or -1. Therefore, all cases of S_{vcr} can be summarized as Table 3. This process may take 1 or 2 cycles to detect the OCF.
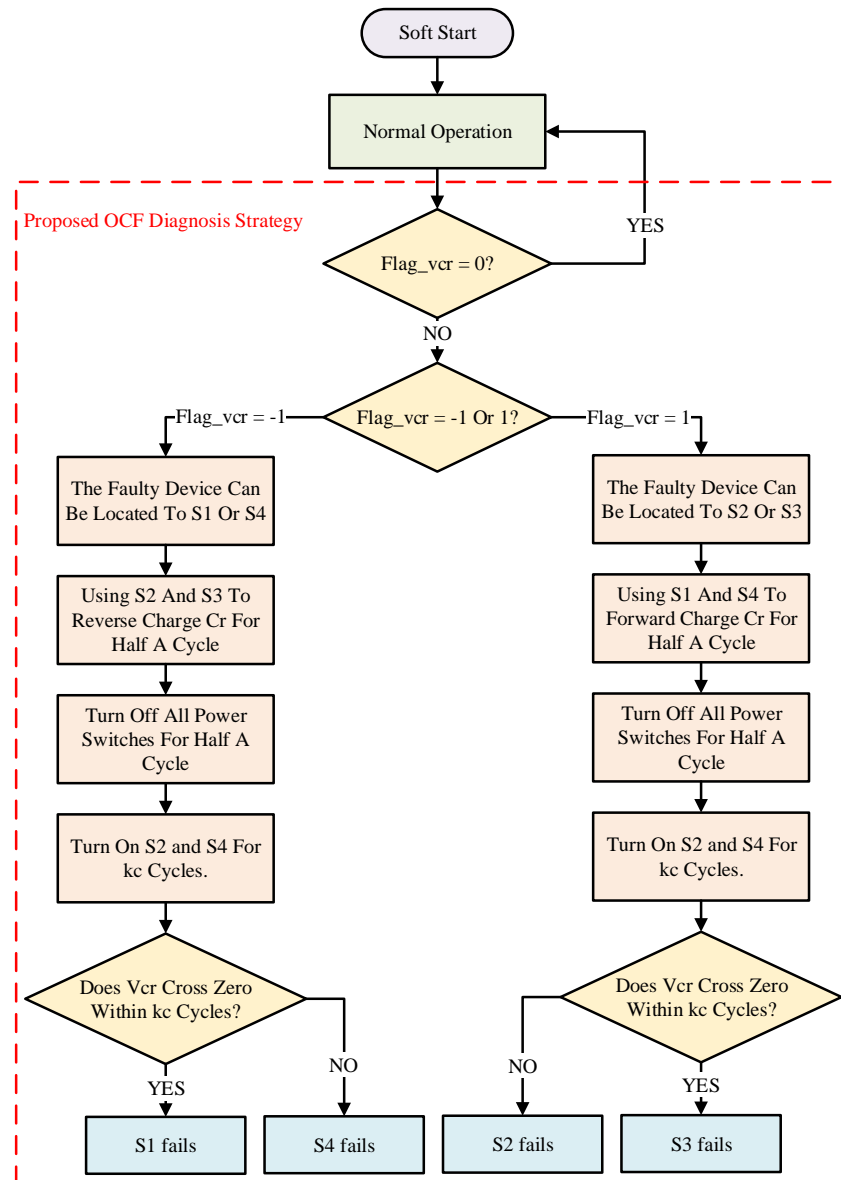
Figure 6. Proposed fault diagnosis strategy.

Table 1. Converter parameters.

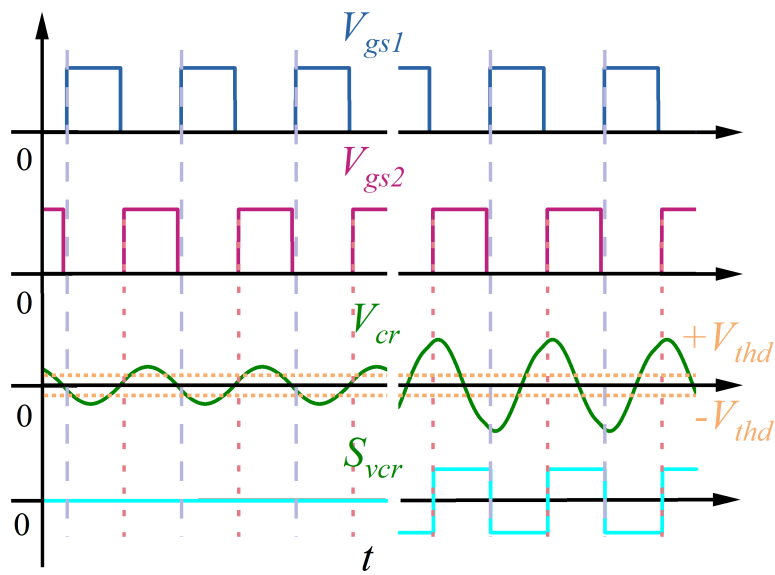|	
Input Voltage V_{in}	36 V
Output Voltage V_o	24 V
Output Power P_o	160 W
Switching Frequency of LLC f_l	200 kHz
Transformer Turns Ratio N	3:2
Magnetizing Inductance L_m	12.5 µH ± 10%
Resonant Inductance L_r	1.8 µH ± 10%
Resonant Capacitance C_r	300 nF ± 5%
MOSFET $S_1 - S_4$	BSC070N10NS3G

Figure 7. Sampling and processing of fault signal.

Table 2. The value of S_{vcr} with the system in condition.

V_{cr}	S_{vcr}
$V_{cr}(t_{beg1})$	-1 or 0
$V_{cr}(t_{beg2})$	1 or 0

Table 3. The relationship between system condition and S_{vcr}.

S_{vcr1} & S_{vcr2}	$flag_{vcr}$	Location of the Fault
1 , 1	1	S_2 or S_3
-1 , -1	-1	S_1 or S_4
else	0	none

However, it is not enough just to detect the OCF, but also to be able to locate the faulty device in some applications such as fault-tolerant methods. Therefore, the operation principles after the OCF should be modified. As shown in Table 3, when $flag_{vcr}$ becomes -1, it can only be determined that the OCF is on S_1 or S_4. Therefore, assuming the OCF on S_1 or S_4 is detected in the k_th cycle, $V_{gs1,4}$ are pulled down and $V_{gs2,3}$ are pulled up in the first half of the $(k+1)\_th$ cycle to charge the C_r. In the second half cycle, all driver signals are pulled down and i_r rapidly drops to 0. Then, $V_{gs2,4}$ are pulled up and $V_{gs1,3}$ are pulled down from the $(k+2)\_th$ cycle to determine whether the OCF is on S_4 or not. In this case, if the faulty device is S_4, only S_2 can be turned on. V_{cr} will remain negative and i_r will remain 0. On the contrary, if the faulty device is S_1, then the resonant tank starts resonance through $S_{2,4}$, and V_{cr} will cross zero point in a few cycles. The number of cycles depends on the ratio of L_m to L_r. The resonant period T_{rf} becomes $\sqrt{(L_r + L_m)C_r}$. Assuming $h = L_m/L_r$, T_{rf} is $\sqrt{1+h}$ times of T_s, which is $T_{rf} = \sqrt{1+h}T_s$. Therefore, V_{cr} will reverse in half a resonant period T_{rf}. Suppose k_c is the rounded up value of $\sqrt{1+h}/2$. According to Table 1, $h = 12.5/1.8 = 6.94$, so $k_c = 2$. From the $(k+2)\_th$ cycle, the system still samples V_{cr} twice every cycle, with a maximum of k_c cycles taken. Therefore, during the $(k+2)\_th$ to $(k+4)\_th$ cycle, once S_{vcr1} or S_{vcr2} changes from -1 to 0 or 1, the faulty device can be proved to be S_1. As shown in Figure 8a, V_{cr} crosses zero and reverses within

one switching cycle as analyzed. On the other hand, S_{vcr} remains -1 until $(k+4)\_th$ cycle as shown in Figure 8b, locating the faulty device at S_4.
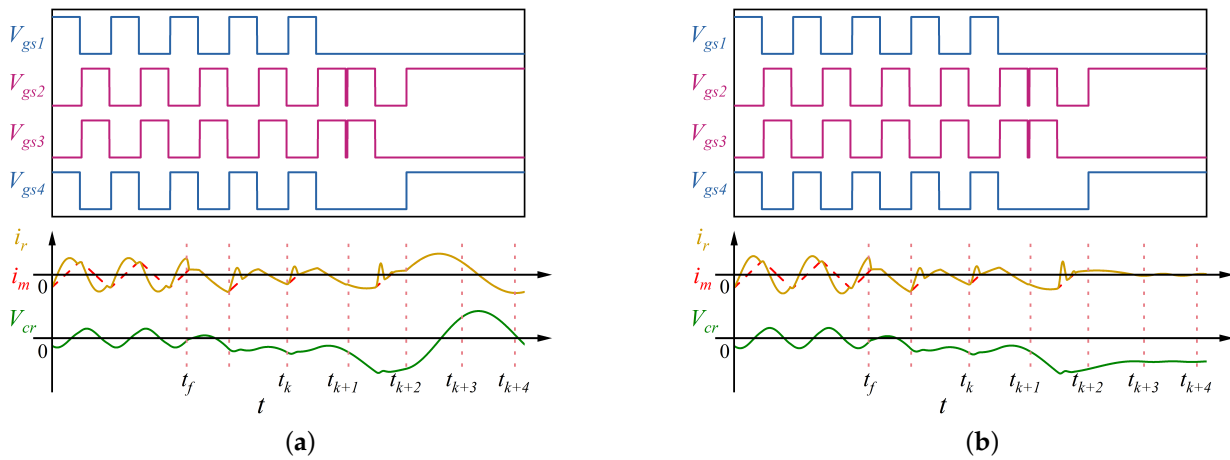

Figure 8. Simulation results of fault diagnosis process with $flag_{vcr} = -1$: (**a**) an OCF on S_1 (**b**) an OCF on S_4.

When $flag_{vcr}$ is 1, the operation principles are the opposite. The OCF on S_2 or S_3 is detected in the k_th cycle. $V_{gs2,3}$ are pulled up and $V_{gs1,4}$ are pulled down in the first half of the $(k+1)\_th$ cycle to charge the C_r. In the second half cycle, all driver signals are pulled down to reduce the amplitude of i_r. Then, $V_{gs2,4}$ are pulled up and $V_{gs1,3}$ are pulled down from the $(k+2)\_th$ cycle to determine whether the OCF is on S_2 or not. From the $(k+2)\_th$ cycle, the system still samples V_{cr} twice every cycle until k_c times. If S_{vcr} is always 1 until $(k+4)\_th$ cycle as shown in Figure 9a, the faulty device is S_2. On the other hand, if S_{vcr} changes from 1 to 0 or -1 as shown in Figure 9b, which proves the faulty device is S_3. In this way, the faulty device can be located and subsequent fault-tolerant methods can be implemented.
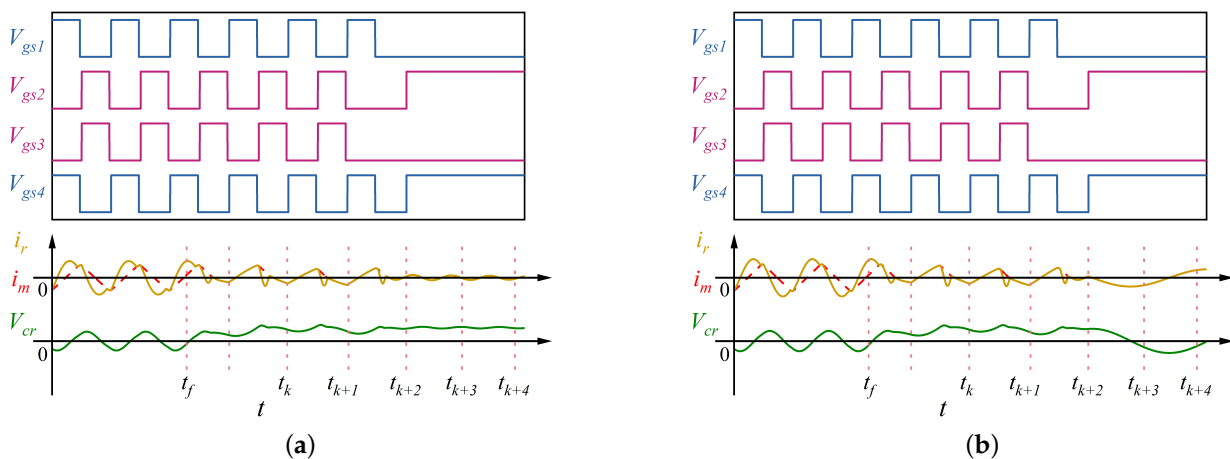

Figure 9. Simulation results of fault diagnosis process with $flag_{vcr} = 1$: (**a**) an OCF on S_2 (**b**) an OCF on S_3.

In some applications, the switching frequency of the converter may be further increased, when the controller may have difficulty maintaining sampling per cycle. In this case, the sampling period can be increased to a multiple of the switching period to save resources. As shown in Figure 10, when the system operates in condition, V_{cr} is sampled every two cycles to save resources for the control method. When an OCF is detected, the control method is stopped and resources are used to locate the OCF as soon as possible.
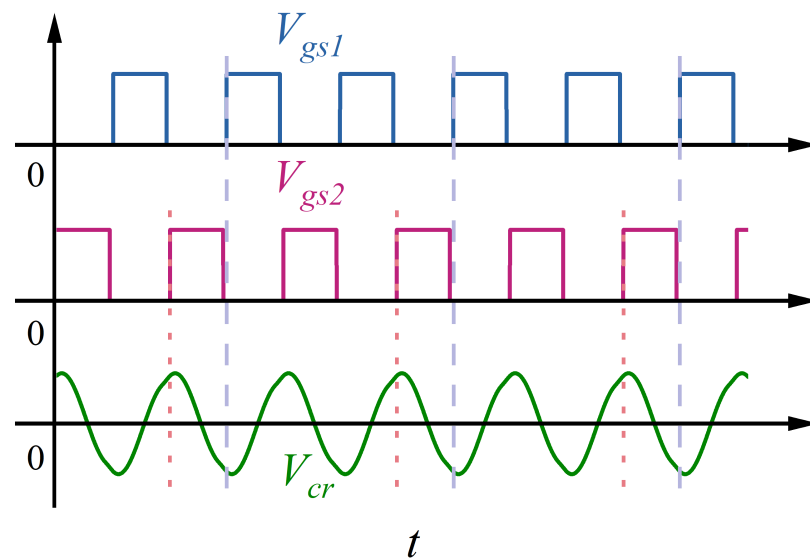
Figure 10. Reducing sampling frequency in high-frequency applications.

4. Experiment Result

To verify the effectiveness of the proposed fault diagnosis method, an LLC converter with parameters shown in Table 1 is built and shown in Figure 11a. The proposed fault diagnosis method is implemented on the DSP TMS320F28377D, a product of Texas Instruments, headquartered in Dallas, TX, USA. The TCPA300 current probe, a Tektronix product based in Beaverton, OR, USA, is utilized for current measurements. The waveforms are monitored using the ZDL6000 wavescope platform, a product of Guangzhou Zhiyuan Electronics Co., Ltd., based in Guangzhou, China.
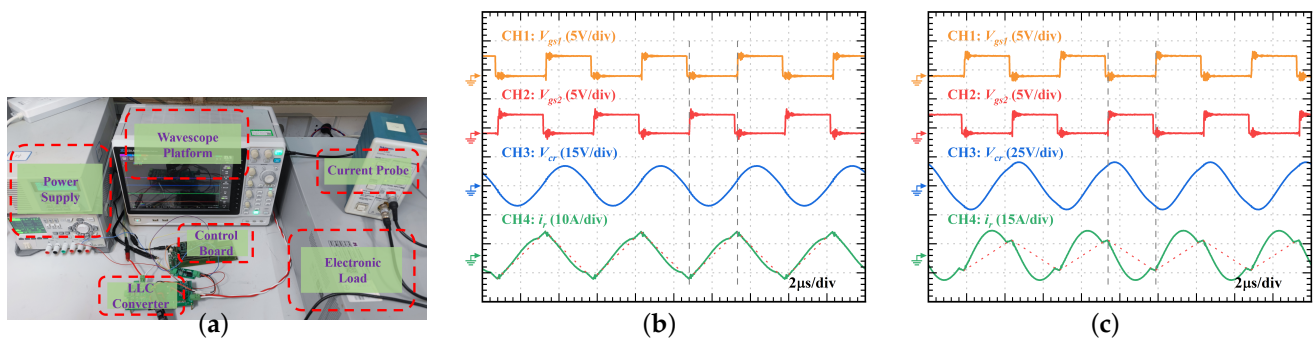

Figure 11. Experimental results of steady-state operation: (**a**) experimental prototype and equipment; (**b**) at 20 W; (**c**) at 120 W.

The relationship between V_{cr} and the sampling time in different loads is shown in Figure 11b,c . The red dotted line next to the solid green line representing i_r is the estimated i_m. The gray dashed lines represent the rising edge moments of V_{gs1} and V_{gs2}. As analyzed, when the load is lighter, i_r and i_m are closer, and V_{cr} at the rising edge of the pulses is closer to 0. On the contrary, when the load is heavy, i_r will quickly cross zero, and V_{cr} at the rising edge will be close to the maximum value of V_{cr}.

The process of detecting and locating OCFs in every power device of the converter is shown Figures 12–14. Among them, the signal T_{ocf} is generated by GPIO, which is used to indicate the time of fault occurrence and diagnosis process. To avoid misjudgment of OCFs, the voltage threshold V_{th} is set to 0.5V. Take the power device S_1 as an example to illustrate. As shown in Figure 12a,b, an OCF occurs on S_1 at $t = t_0$, and T_{ocf} is pulled up. In the process of $t_0 - t_1$, the system detects that $flag_{vcr}$ is -1, judges that there is an OCF on S_1 or S_4, and starts to locate the faulty device. At $t = t_1$, V_{gs2} and V_{gs3} are pulled up, the

power supply charges C_r through S_2 and S_3, which make the amplitude of V_{cr} rises rapidly. At $t = t_2$, V_{gs2} and V_{gs3} are pulled down, S_{1-4} are all turned off, the resonant current ir quickly drops to 0, and V_{cr} also remains stable, preparing for the subsequent i_r direction reversal to make V_{cr} quickly cross zero. From $t = t_3$, V_{gs2} and V_{gs4} are pulled up, and V_{cr} is continuously sampled to determine whether V_{cr} will be close to zero or cross zero within kc cycles, that is, before time t_4. S_2 and S_4 are healthy and form a resonant circuit, and i_r has dropped to 0 before $t = t_3$. After $t = t_3$, i_r rises rapidly, causing V_{cr} to rise rapidly, and crosses zero after about half a cycle, which makes the system locate the faulty device S_1.
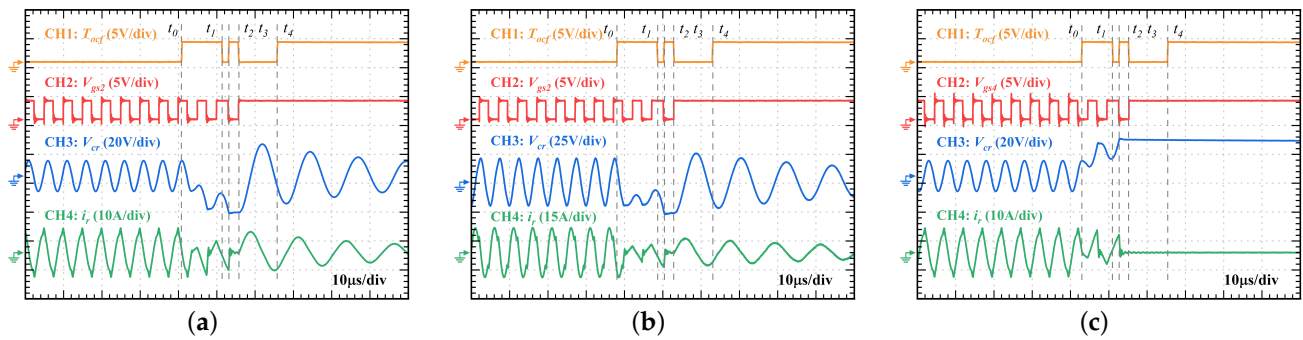

Figure 12. Experimental results of steady-state operation: (**a**) an OCF on S_1 at 20 W; (**b**) an OCF on S_1 at 120 W; (**c**) an OCF on S_2 at 20 W.
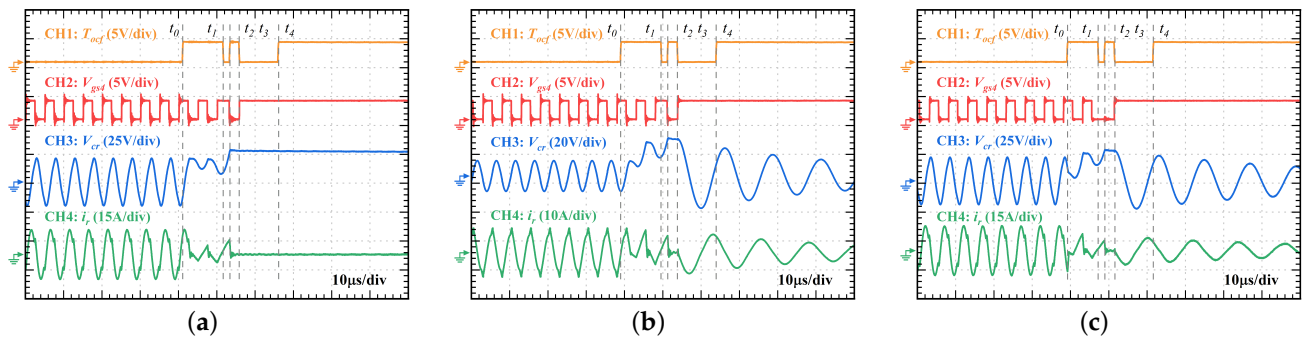

Figure 13. Experimental results of steady-state operation: (**a**) an OCF on S_2 at 120 W; (**b**) an OCF on S_3 at 20W; (**c**) an OCF on S_3 at 120 W.
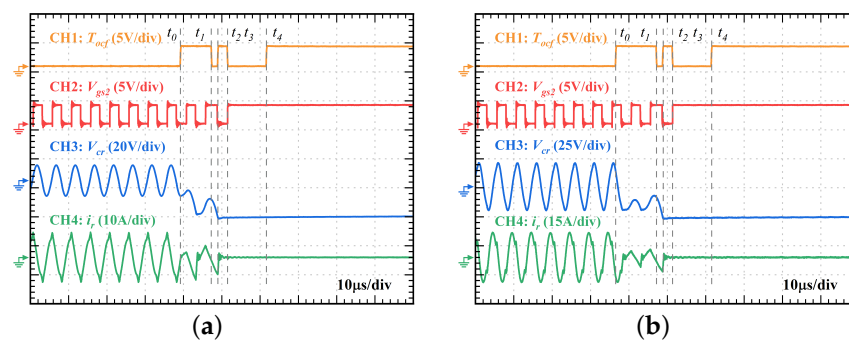

Figure 14. Experimental results of steady-state operation: (**a**) an OCF on S_4 at 20 W; (**b**) an OCF on S_4 at 120 W.

The detection and location process of S_2 is shown in Figures 12c and 13a. At $t = t_0$, the power device S_2 has an OCF. The system detects that $flag_{vcr}$ is 1, and judges that S_2 or S_3 is faulty. Therefore, the system pulls up V_{gs1} and V_{gs4} at $t = t_1$, uses S_1 and S_4 to charge C_r, and turns off all power devices at $t = t_2$, so that the resonant current i_r drops to 0 until $t = t_3$. At $t = t_3$, S_2 and S_4 are turned on and V_{cr} is continuously detected. However, due

to the OCF of S_2, the resonant circuit cannot be formed, and V_{cr} hardly changes. Until $t = t_4$, V_{cr} is still not close to zero or crosses zero, so the faulty device is located as S_2.

The diagnosis processes of S_3 and S_4 are similar to the above and are shown in Figures 13 and 14. According to the fault diagnosis processes of various power devices, the detection process of the proposed fault diagnosis method needs 1–2 switching cycles, and locates the faulty device within a maximum of 3 switching cycles.

5. Conclusions

In this paper, an OCF diagnosis method for LLC converters is proposed. The proposed diagnosis method can locate the faulty switch within the system in 30 µs, and can be extended to high-frequency applications. The direction of V_{cr} is utilized to detect the OCF. Then, the fault injection strategy is adopted to locate the faulty device. The proposed diagnostic technique requires only a single voltage sensor, a component already incorporated in numerous control method converters. This represents a reduction from the 2–3 sensors typically required. Furthermore, it outperforms conventional methods by reducing the number of samples to 1–2 per switch cycle. The diagnostic time has been reduced from over 70 µs to less than 30 µs, thereby facilitating swift OCF detection.

Author Contributions: Methodology, S.X.; Validation, W.W. and P.Z.; Formal analysis, W.W.; Investigation, Y.P.; Resources, W.L.; Data curation, P.Z.; Writing—review & editing, S.X.; Supervision, Y.L.; Funding acquisition, W.L. All authors have read and agreed to the published version of the manuscript.

Data Availability Statement: Data are contained within the article.

References

1. Pei, X.; Nie, S.; Chen, Y.; Kang, Y. Open-Circuit Fault Diagnosis and Fault-Tolerant Strategies for Full-Bridge DC–DC Converters. *IEEE Trans. Power Electron.* **2012**, *27*, 2550–2565. [CrossRef]
2. Soon, J.L.; Lu, D.D.C.; Peng, J.C.H.; Xiao, W. Reconfigurable Nonisolated DC–DC Converter with Fault-Tolerant Capability. *IEEE Trans. Power Electron.* **2020**, *35*, 8934–8943. [CrossRef]
3. Rastogi, S.K.; Shah, S.S.; Singh, B.N.; Bhattacharya, S. Mode Analysis and Identification Scheme of Open-Circuit Fault in a Three-phase DAB Converter. In Proceedings of the 2021 IEEE Energy Conversion Congress and Exposition (ECCE), Virtual, 10–14 October 2021; pp. 2762–2769. [CrossRef]
4. Ferreira Costa, L.; Liserre, M. Failure Analysis of the dc-dc Converter: A Comprehensive Survey of Faults and Solutions for Improving Reliability. *IEEE Power Electron. Mag.* **2018**, *5*, 42–51. [CrossRef]
5. Patel, K.; Borole, S.; Manikandan, R.; Singh, R.R. Short Circuit and Open Circuit Fault Identification Strategy for 3-Level Neutral Point Clamped Inverter. In Proceedings of the 2021 Innovations in Power and Advanced Computing Technologies (i-PACT), Kuala Lumpur, Malaysia, 27–29 November 2021; pp. 1–6. [CrossRef]
6. Yin, H.; Chen, Q.; Guo, X.; Qiu, X.; Duan, X.; Zhao, X. Fast Open-Switch Fault Diagnosis Based on Model Reference Adaptive Theory Applied to Inverter System. In Proceedings of the 2022 12th International Conference on Power and Energy Systems (ICPES), Guangzhou, China, 23–25 December 2022; pp. 890–895. [CrossRef]
7. Ahmad, M.W.; Gorla, N.B.Y.; Malik, H.; Panda, S.K. A Fault Diagnosis and Postfault Reconfiguration Scheme for Interleaved Boost Converter in PV-Based System. *IEEE Trans. Power Electron.* **2021**, *36*, 3769–3780. [CrossRef]
8. Xu, L.; Ma, R.; Xie, R.; Xu, J.; Huangfu, Y.; Gao, F. Open-Circuit Switch Fault Diagnosis and Fault- Tolerant Control for Output-Series Interleaved Boost DC–DC Converter. *IEEE Trans. Transp. Electrif.* **2021**, *7*, 2054–2066. [CrossRef]
9. Kumar, M. Open Circuit Fault Detection and Switch Identification for LS-PWM H-Bridge Inverter. *IEEE Trans. Circuits Syst. II Express Briefs* **2021**, *68*, 1363–1367. [CrossRef]
10. Ding, X.; Wang, B.; Yang, Y. DC Power Cycling Test and Lifetime Prediction for SiC MOSFETs. In Proceedings of the 2023 26th International Conference on Electrical Machines and Systems (ICEMS), Guangdong, China, 5–8 November 2023; pp. 4638–4643. [CrossRef]
11. Givi, H.; Farjah, E.; Ghanbari, T. A Comprehensive Monitoring System for Online Fault Diagnosis and Aging Detection of Non-Isolated DC–DC Converters' Components. *IEEE Trans. Power Electron.* **2019**, *34*, 6858–6875. [CrossRef]
12. Dusmez, S.; Duran, H.; Akin, B. Remaining Useful Lifetime Estimation for Thermally Stressed Power MOSFETs Based on ON-State Resistance Variation. *IEEE Trans. Ind. Appl.* **2016**, *52*, 2554–2563. [CrossRef]

13. Zhuo, S.; Xu, L.; Gaillard, A.; Huangfu, Y.; Paire, D.; Gao, F. Robust Open-Circuit Fault Diagnosis of Multi-Phase Floating Interleaved DC–DC Boost Converter Based on Sliding Mode Observer. *IEEE Trans. Transp. Electrif.* **2019**, *5*, 638–649. [CrossRef]
14. Bento, F.; Marques Cardoso, A.J. Open-circuit fault diagnosis in interleaved DC-DC boost converters and reconfiguration strategy. In Proceedings of the 2017 IEEE 11th International Symposium on Diagnostics for Electrical Machines, Power Electronics and Drives (SDEMPED), Tinos, Greece, 29 August–1 September 2017; pp. 394–400. [CrossRef]
15. Chen, L.; Zhao, X.; Tang, S.X. Online Fault Diagnosis Method for High-Performance Converters Using Inductor Voltage Polar Signatures. *IEEE Access* **2020**, *8*, 179778–179788. [CrossRef]
16. Ribeiro, E.; Cardoso, A.J.M.; Boccaletti, C. Open-Circuit Fault Diagnosis in Interleaved DC–DC Converters. *IEEE Trans. Power Electron.* **2014**, *29*, 3091–3102. [CrossRef]
17. Poon, J.; Jain, P.; Konstantakopoulos, I.C.; Spanos, C.; Panda, S.K.; Sanders, S.R. Model-Based Fault Detection and Identification for Switching Power Converters. *IEEE Trans. Power Electron.* **2017**, *32*, 1419–1430. [CrossRef]
18. Poon, J.; Jain, P.; Spanos, C.; Panda, S.K.; Sanders, S.R. Fault Prognosis for Power Electronics Systems Using Adaptive Parameter Identification. *IEEE Trans. Ind. Appl.* **2017**, *53*, 2862–2870. [CrossRef]
19. He, X.; Ren, H.; Han, P.; Chen, Y.; Shu, Z.; He, X. Open Circuit Fault Diagnosis of Advanced Cophase Traction Power Supply System Based on Neural Network. In Proceedings of the 2018 International Conference on Intelligent Rail Transportation (ICIRT), Singapore, 12–14 December 2018; pp. 1–5. [CrossRef]
20. Gou, B.; Xu, Y.; Xia, Y.; Wilson, G.; Liu, S. An Intelligent Time-Adaptive Data-Driven Method for Sensor Fault Diagnosis in Induction Motor Drive System. *IEEE Trans. Ind. Electron.* **2019**, *66*, 9817–9827. [CrossRef]
21. Shi, H.; Wen, H.; Li, J. Fault Analysis and Fault-Tolerant Method of Dual Active Bridge Converter under Triple Phase Shift Control. In Proceedings of the 2019 10th International Conference on Power Electronics and ECCE Asia (ICPE 2019-ECCE Asia), Busan, Republic of Korea, 27–30 May 2019; pp. 1121–1127. [CrossRef]
22. Hu, Z.; Liu, Y.F.; Sen, P.C. Bang-Bang Charge Control for LLC Resonant Converters. *IEEE Trans. Power Electron.* **2015**, *30*, 1093–1108. [CrossRef]
23. Fei, C.; Ahmed, M.H.; Lee, F.C.; Li, Q. Two-Stage 48 V-12 V/6 V-1.8 V Voltage Regulator Module With Dynamic Bus Voltage Control for Light-Load Efficiency Improvement. *IEEE Trans. Power Electron.* **2017**, *32*, 5628–5636. [CrossRef]